universe

MDPI

Review

Anisotropic Compact Stars: Theory and Simulation from Microphysical Models to Macroscopic Structure and Observables

Zenia Zuraiq [1], Mayusree Das [2], Debabrata Deb [3,4], Surajit Kalita [5], Fridolin Weber [6,7] and Banibrata Mukhopadhyay [1,2,*]

1 Department of Physics, Indian Institute of Science, Bangalore 560012, India; zeniazuraiq@iisc.ac.in
2 Joint Astronomy Programme, Indian Institute of Science, Bangalore 560012, India; mayusreedas@iisc.ac.in
3 Centre for Space Research, North-West University, Private Bag X6001, Potchefstroom 2520, South Africa; d.deb32@gmail.com
4 National Institute for Theoretical and Computational Sciences (NITheCS), Stellenbosch 7604, South Africa
5 Astronomical Observatory, University of Warsaw, Al. Ujazdowskie 4, 00-478 Warszawa, Poland; skalita@astrouw.edu.pl
6 Department of Physics, San Diego State University, 5500 Campanile Drive, San Diego, CA 92182, USA; fweber@ucsd.edu
7 Center for Astrophysics and Space Sciences, University of California at San Diego, La Jolla, CA 92093, USA
* Correspondence: bm@iisc.ac.in

Abstract

Strong magnetic fields and anisotropic stresses can substantially modify the structure and observable properties of compact stars. In this review, we present a unified treatment of magnetically induced anisotropy across neutron stars, hybrid stars, and white dwarfs, connecting the microphysical equation of state effects to macroscopic structure and multimessenger observables. We demonstrate that magnetic-field geometry plays a decisive role: toroidally oriented (transverse) fields enhance the maximum mass by providing additional perpendicular pressure support, whereas radially oriented fields primarily increase central compression with comparatively small mass gain. In neutron stars, anisotropy and magnetic stresses can shift phase-transition thresholds in hybrid models and enable configurations in the lower mass gap with significantly smaller magnetic energy compared to the gravitational binding energy. We further show that continuous gravitational wave emission from magnetically deformed neutron stars provides a complementary probe of internal field geometry through ellipticity-driven strain evolution. In magnetized white dwarfs, super-Chandrasekhar masses arise from the spatial redistribution of magnetic stresses rather than from globally strong magnetic energy. Taken together, these results highlight that magnetic-field geometry and matter anisotropy are as important as field strength in determining mass–radius relations, tidal deformability, gravitational wave detectability, and the emergence of extreme compact-star configurations.

Keywords: anisotropy; magnetic fields; neutron stars; gravitational waves; tidal deformability

Check for updates

Academic Editors: Efrain J. Ferrer, Vivian de la Incera and Cristina Manuel

Received: 31 March 2026
Revised: 24 April 2026
Accepted: 28 April 2026
Published: 30 April 2026

Copyright: © 2026 by the authors. Licensee MDPI, Basel, Switzerland. This article is an open access article distributed under the terms and conditions of the Creative Commons Attribution (CC BY) license.

1. Introduction

Compact stars, including white dwarfs (WDs) and neutron stars (NSs), represent natural laboratories for exploring matter under extreme conditions of density, gravity, and magnetic fields. These objects probe regimes where quantum mechanics, general relativity (GR), and nuclear physics intersect, making them crucial for testing fundamental theories of physics. In particular, strongly magnetized compact stars, such as magnetars

(highly magnetized NSs) and highly magnetized WDs, have attracted considerable attention due to their observational signatures and theoretical implications.

Observations over the past two decades have revealed the existence of NSs with surface magnetic fields reaching 10^{14}–10^{15} G [1], as well as WDs exhibiting magnetic fields as high as 10^{9} G at the surface [2] and potentially much stronger fields in their interiors [3]. Such intense magnetic fields are expected to modify the internal structure of compact stars in a nontrivial manner. One of the most important consequences of strong magnetization is the emergence of pressure anisotropy: the pressure perpendicular to the magnetic field differs from that parallel to it. This anisotropy arises naturally due to the breaking of spatial isotropy by the magnetic field and has profound implications for stellar equilibrium, stability, and mass–radius ($M - R$) relations.

Traditional models of compact stars often assume isotropic pressure and spherical symmetry, leading to the well-known Tolman–Oppenheimer–Volkoff (TOV) equations for hydrostatic equilibrium in GR. However, when strong magnetic fields are present, this assumption becomes questionable. The magnetic field contributes both to the energy density and to anisotropic stresses through the electromagnetic (EM) energy–momentum tensor.

Apart from magnetic field, other physical mechanisms may also lead to anisotropy [4], e.g., formation of exotic states in NS cores such as pion condensates or superfluid neutrons, proton and color superconducting phases [5–7], and the presence of two (or more) fluids (see [8] for a complete review of the possible origin(s) of pressure anisotropy within compact stars). Additionally, the dynamic process of stellar evolution brings with it processes including shear viscosity, heat conduction, and other non-adiabatic transport phenomena, which further generate pressure anisotropy in the star [9]. Consequently, the equilibrium configuration of such stars must be described within a framework that consistently incorporates anisotropic pressure and magnetic field effects (see, e.g., [4]).

In addition to magnetic anisotropy, several studies have suggested that certain astrophysical observations—such as peculiar over-luminous and under-luminous Type Ia supernovae (SNe Ia) [10,11]—may require compact stars exceeding or falling below traditional mass limits. This has motivated investigations into modified gravity theories (e.g., [12]), exotic equation(s) of state (EoS) (e.g., [13]) and non-standard microphysical effects. In magnetized environments, these considerations become even more intricate, as magnetic pressure, Landau quantization of charged particles [14,15], and field-induced deformation [16,17] collectively influence the macroscopic properties of the star.

The study of magnetic anisotropic compact stars is, therefore, of central importance for understanding their maximum mass, stability criteria, deformation, gravitational wave (GW) emission prospects [18,19], and EM observables. In particular, deviations from isotropy can alter the $M - R$ relation, shift stability boundaries, and potentially lead to observable signatures in GW astronomy and high-energy astrophysics.

In this review, we investigate the structure and properties of compact stars in the presence of strong magnetic fields that induce pressure anisotropy. We develop a self-consistent framework to model the anisotropic energy–momentum tensor and analyze its consequences for equilibrium configurations. Our goal is to quantify how anisotropy due to magnetic field and the matter effect modifies stellar structure and to assess its astrophysical implications.

This review is organized as follows. In Section 2, we outline the theoretical framework and governing equations for magnetized anisotropic NSs and hybrid stars. We explore therein the underlying EoS, $M - R$ relations and implications. In Section 3, we explore the detectability of NSs by their GW signals. Section 4 explores the anisotropic magnetized WDs and their consequences. Finally, in Section 5, we summarize our findings and discuss their broader astrophysical significance.

https://doi.org/10.3390/universe12050130

2. Exploring Anisotropic Neutron Stars and Hybrid Stars

We, in the past, explored anisotropic NSs composed of different EoSs [4,20]. The anisotropy induced by a combination of magnetic-field and matter effects enhances the NS masses through structural effects. In the present work, we revisit the work and its compatibility with different kinds of matter compositions within the NS—i.e., nucleonic matter ($npe\mu$), hyperon-delta admixed stars ($npe\mu - Y\Delta$), as well as hybrid stars with quark matter admixed cores. We also compute the magnetic-to-gravitational ratio ($E_{\rm mag}/E_{\rm grav}$) and tidal deformability to ensure compatibility with observational limits and/or stability.

2.1. Formalism

Following previous work [4,20,21], we solve the stellar structure equations for anisotropic compact stars/NSs in approximate spherical symmetry using the modified Tolman–Oppenheimer–Volkoff (TOV) equations, incorporating anisotropic and/or magnetic effects, given by

$$\frac{\mathrm{d}m}{\mathrm{d}r} = 4\pi r^2\left(\rho + \frac{B^2}{8\pi}\right), \tag{1}$$

$$\frac{\mathrm{d}p_r}{\mathrm{d}r} = \begin{cases} \dfrac{-(\rho+p_r)\dfrac{4\pi r^3\left(p_r-\frac{B^2}{8\pi}\right)+m}{r(r-2m)}+\frac{2}{r}\Delta}{1-\frac{d}{d\rho}\left(\frac{B^2}{8\pi}\right)\left(\frac{d\rho}{dp_r}\right)} & \text{(for RO)}, \\ \dfrac{-(\rho+p_r+\frac{B^2}{4\pi})\dfrac{4\pi r^3\left(p_r+\frac{B^2}{8\pi}\right)+m}{r(r-2m)}+\frac{2}{r}\Delta}{1+\frac{d}{d\rho}\left(\frac{B^2}{8\pi}\right)\left(\frac{d\rho}{dp_r}\right)} & \text{(for TO)}. \end{cases} \tag{2}$$

Here, we consider both radially oriented (RO) and transversely oriented (TO) fields in our work. These are the one-dimensional analogs of poloidal and toroidal magnetic fields, respectively. These equations are supplemented by the profiles for magnetic field [22] and anisotropy [4,23] within the star and EoS. The magnetic field profile is given by

$$B(\rho) = B_s + B_0\left[1 - \exp\left\{-\eta\left(\frac{P}{P_0}\right)^{\gamma}\right\}\right], \tag{3}$$

where B_s, B_0, η and γ are model parameters that control field magnitude and how the field decays from center to surface.

We use a pressure-dependent parameterization for the field instead of the usual density dependence considered in previous work [22]. This enables us to study hybrid stars where phase transitions can lead to large discontinuities in the density within the star, while keeping pressure continuous. Throughout this work, we have chosen B_s to be 10^{15} G for NSs. The results we obtain are independent of this parameter under the assumption that B_s and B_0 are not comparable.

The model anisotropy introduced in Equation (2) is given by the profile [4,23]

$$\Delta = \begin{cases} \kappa r^2\dfrac{(\rho+p_r)\left(\rho+3p_r-\frac{B^2}{4\pi}\right)}{1-\frac{2m}{r}} & \text{(for RO)}, \\ \kappa r^2\dfrac{(\rho+p_r+\frac{B^2}{4\pi})\left(\rho+3p_r+\frac{B^2}{2\pi}\right)}{1-\frac{2m}{r}} & \text{(for TO)}, \end{cases} \tag{4}$$

where κ is constrained by physicality arguments [24] within the star to lie in the range $[-2/3,2/3]$. The anisotropy here is considered to be representing matter and/or magnetic field effects, capturing the effects due to the deviation from spherical symmetry, arising from the various mechanisms mentioned in the Introduction. Note here, however, that our one-dimensional treatment is still valid for the magnetic fields under consideration (central magnetic field, $B_c < 10^{18}$ G). This is also seen in full Einstein–Maxwell solutions of NS

structures, e.g., the XNS code-based results [25]. In particular, toroidally magnetized NSs (corresponding to our TO fields) lead to very little deviation from spherical symmetry.

To ensure physical consistency and dynamical plausibility, we require the magnetic energy to remain well below the gravitational binding energy, i.e., $E_{\rm mag}/|E_{\rm grav}| \ll 1$. All equilibrium configurations reported here satisfy $E_{\rm mag}/|E_{\rm grav}| \lesssim \mathcal{O}(10^{-2})$ [26], indicating that gravity dominates the global energetics and that the magnetic field primarily redistributes internal stresses rather than providing overall support. We additionally impose the tidal deformability constraints inferred from GW170817, namely $\Lambda_{1.4} < 580$ [27] (with the less restrictive bound $\Lambda_{1.4} < 800$ [28]).

2.2. Equation of State

We choose a selection of phenomenological EoS constructed using the relativistic mean field (RMF) approach. More specifically, we examine the DDMEX [29], DD2 [30], and DDME2 [31] EoS.

Purely nucleonic cases ($npe\mu$)

We initially look at purely nucleonic cases ($npe\mu$ matter). The mass-radius ($M-R$) curves for the given EoS are shown in Figure 1. The corresponding dimensionless tidal deformability parameter Λ is shown as a function of the mass M in the inset.

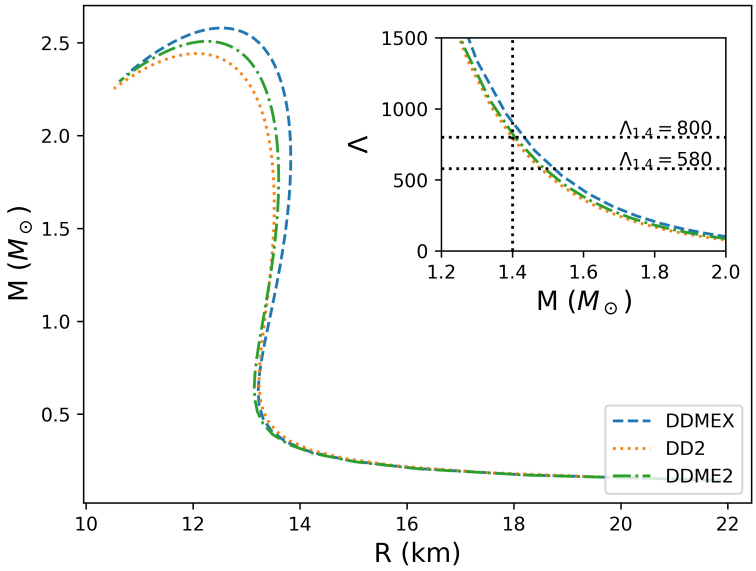


Figure 1. $M-R$ curves for 3 purely nucleonic EoSs: DDMEX, DD2, and DDME2. The tidal deformabilities are shown in the inset, along with the limits from GW170817.

Evidently, all the purely nucleonic cases, although having maximum mass ($M_{\rm max}$) of 2.5 $M_\odot$ and higher, are ruled out as they do not conform to the tidal deformability constraint. However, the presence of anisotropy can change the situation. Due to the strong dependence of Λ on the compactness of the star ($\Lambda \propto (R/M)^5$), anisotropic stars have a better chance of complying with the tidal deformability constraint, both with and without the magnetic field. This is shown in Figure 2 in the case of the DDMEX EoS. Similar effects were previously explored in our magnetic, anisotropic model [20].

However, we also know from energetic arguments that exotic phases (e.g., hyperons, deconfined quarks) are expected to arise at the high densities of NS cores; hence, these might not be the most ideal candidates.

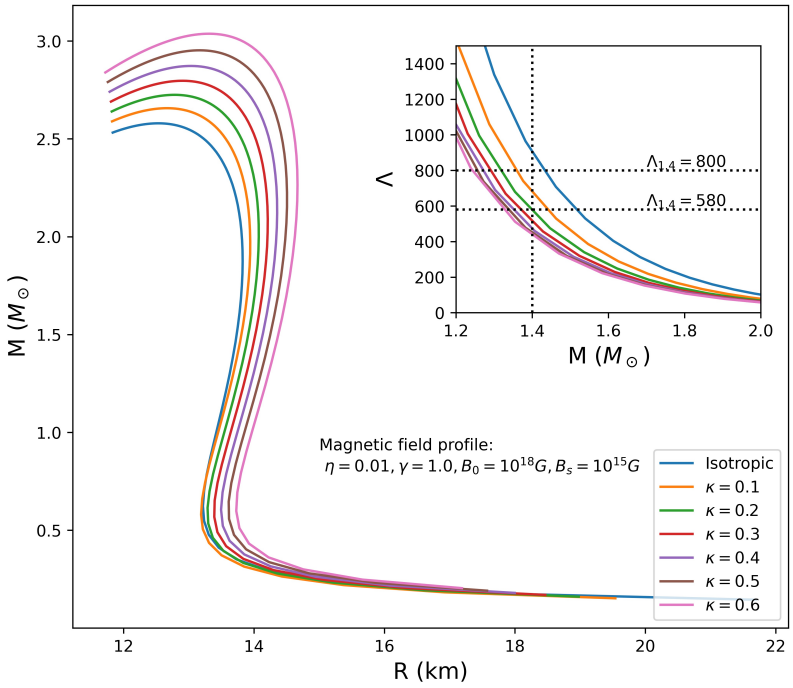


Figure 2. $M - R$ curves for varying κ for the nucleonic DDMEX EoS. The tidal deformabilities are shown in the inset, along with the limits from GW170817.

Hyperon-delta ($npe\mu - Y\Delta$) admixed

We next look at the cases with hyperons and delta particles admixed at high densities. These are expected to arise in the star based on energetic arguments.

We see that the hyperon cases, even in the isotropic regime, satisfy the tidal deformability limits discussed previously. However, "hyperon softening" leads stars to attain masses lower than the mass gap.

In the presence of anisotropy and magnetic fields, the underlying mass limits change. We find that in the presence of a positive anisotropy term, κ tends to increase the mass of the star. If this anisotropic star further has RO fields, they tend to decrease its mass, whereas TO fields tend to increase the mass. Hence, the field geometry and magnitude both play a role in the eventual fate of the star. These results in the case of the DDMEX EoS (the stiffest EoS in our selection) are shown in Figure 3.

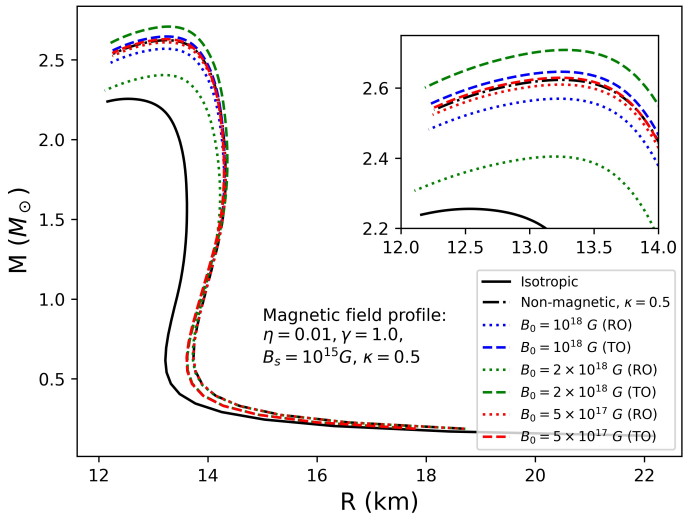


Figure 3. *Cont.*

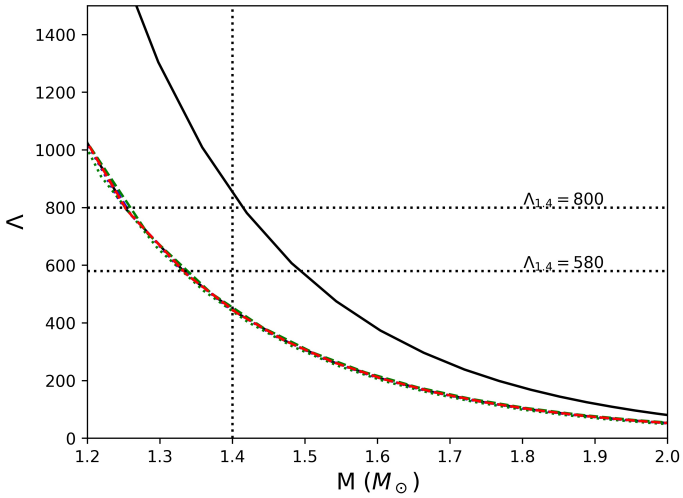


Figure 3. (**Upper**): $M - R$ curves for DDMEX with hyperon-delta admixed EoS for anisotropic stars of varying magnetic field strengths by different B_0 with a fixed $\kappa = 0.5$ and the field profile parameters $\eta = 0.01, \gamma = 1$. (**Lower**): Λ as a function of M for the various cases.

Further, as in the nucleonic case, the tidal deformability is very strongly related to the degree of anisotropy in the star. Higher κ leads to lower $\Lambda_{1.4}$, making the star more compliant with the existing limits. This effect is shown in Figure 4.

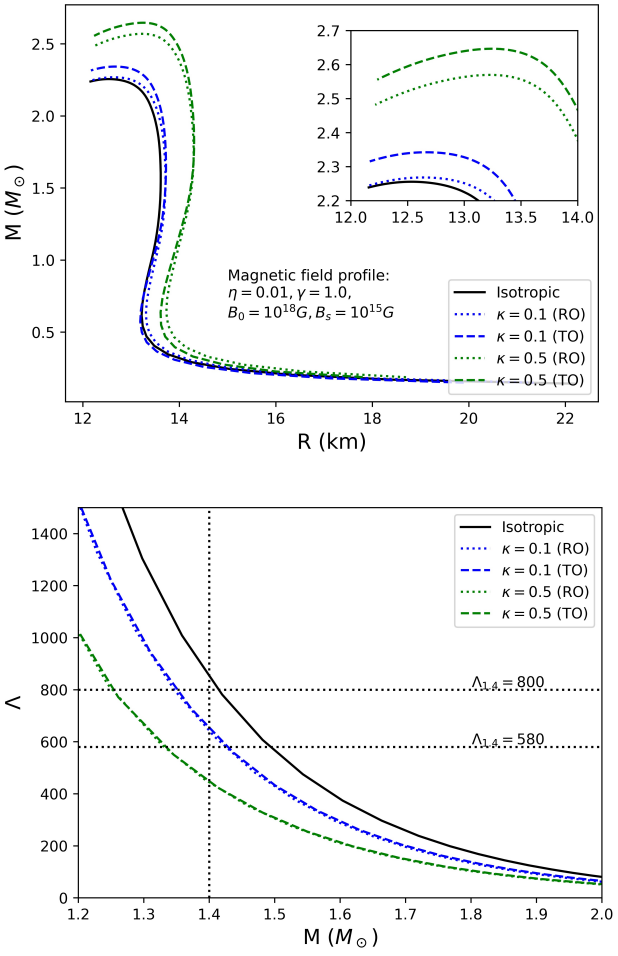


Figure 4. (**Upper**): $M - R$ curves for DDMEX with hyperon-delta admixed EoS for anisotropic stars of varying anisotropic strengths (different κ) with a fixed magnetic field profile parameters $\eta = 0.01, \gamma = 1$ and $B_0 = 10^{18}$ G. (**Lower**): Λ as a function of M for the various cases.

2.3. Hybrid Stars

Another intriguing possibility is that of a deconfined quark phase. At the high densities of NS cores, there could be a phase transition (PT) that converts the nucleonic/hyperonic matter to deconfined quark matter. It has long been hypothesized that a more extreme possibility could arise wherein the deconfined quark phase is absolutely stable, leading to self-bound strange stars. Here, we look at a less extreme scenario where only the core of the star undergoes a PT, i.e., where quark matter is only stabilized at high pressures, leading to hybrid stars [32].

For our hybrid star analysis, we choose a collection of multi-polytrope EoS, viz., ACB4 and ACB5. Here we further consider the models including the Δ_p parameter [33], which controls the degree of discontinuity associated with the PT—larger Δ_p indicates a smoother transition from the hadronic phase to the quark phase, indicating the presence of a mixed phase. ACB4 undergoes a PT at 2 $M_\odot$, whereas ACB5 does so at 1.4 $M_\odot$. Figure 5 shows the behavior of these EoS and the underlying PTs for different Δ_p values.

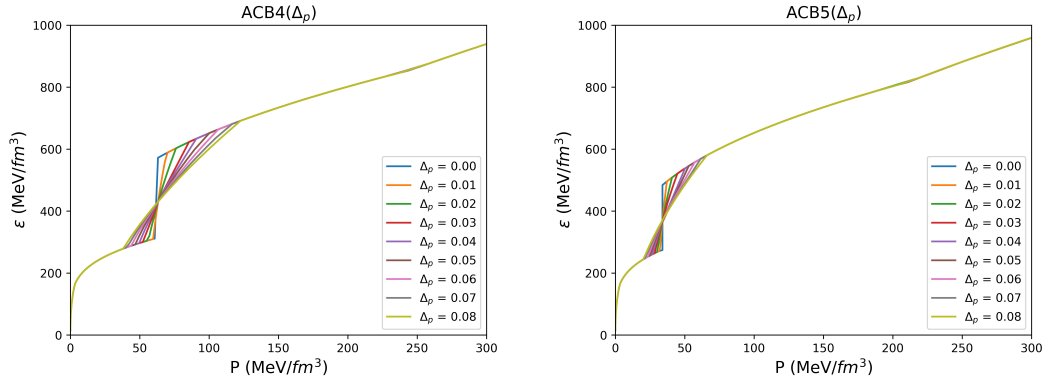


Figure 5. (**Left panel**): ACB4 EoSs, with different values of Δ_p, where increasing Δ_p indicates additional pressure added to the mixed phase. (**Right panel**): the same as the left panel but for ACB5 EoS.

We next examine the effects of anisotropy and magnetic fields in these hybrid stars. As mentioned previously, we choose a pressure parameterization for the magnetic field, as this minimizes errors due to discontinuities in the density profile during a PT.

As shown in Figure 6, we see similar trends as in the previous cases (see Figures 2 and 4). We particularly focus on the toroidally oriented magnetic fields, as these are the cases that give high masses.

The effect of anisotropy on the hadronic branch (the initial rise of M with increasing R) is significantly stronger than that on the quark branch (e.g., the mass change from 2–2.7 $M_\odot$ in the former, compared to 2.1–2.4 $M_\odot$ in the latter in the upper panel of Figure 6). This difference arises because the quark phase emerges at higher densities, where the relative contribution of the magnetic field to the total pressure is smaller. Consequently, magnetic anisotropy primarily modifies the intermediate-density hadronic regime and shifts the mass at which PT occurs in $M - R$ space.

In this framework, the combined action of magnetic stresses and matter anisotropy raises the maximum mass of the hadronic branch before the quark core becomes energetically favorable. Hybrid stars constructed within our magnetic, anisotropic model can, therefore, reach masses in the lower mass gap without requiring the quark phase itself to provide the dominant mass enhancement.

The presence of mixed phase tends to make the PT softer and, as such, the effect of anisotropy at the point of PT is not as significant for higher Δ_p, as shown by Figure 7. It is important to note here that $\Delta_p = 0$ corresponds to the sharpest PT, which corresponds

to a Maxwell construction. As shown previously [34], however, even moderate values of surface tension between the two phases can disfavor the formation of a mixed phase.

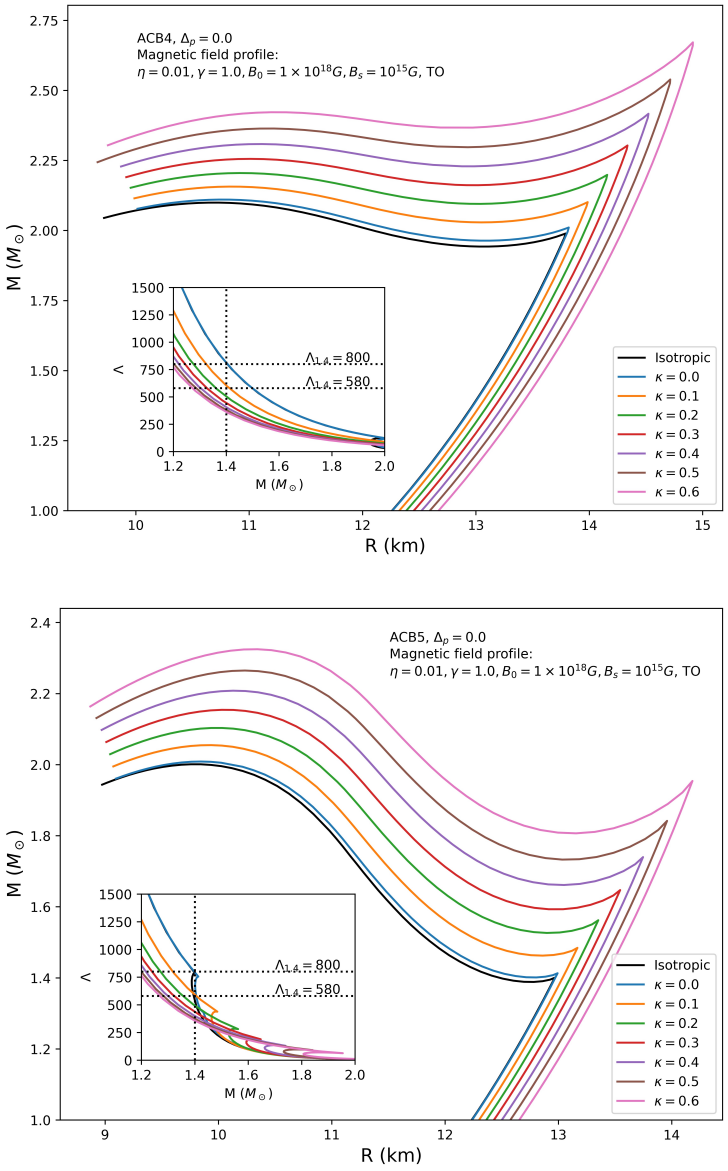


Figure 6. (**Upper**): $M - R$ curves for hybrid stars with the EoS: ACB4 and $\Delta_p = 0.0$ with varying κ. The magnetic field parameters are fixed to $\eta = 0.01, \gamma = 1$ and $B_0 = 10^{18}$ G. Inset shows Λ as a function of M along with the GW170817 limits. (**Lower**): Hybrid stars with the same parameters constructed with the ACB5 EoS and $\Delta_p = 0.0$.

One further possibility not explicitly examined here is the possible emergence of color superconductivity within the star. There are a number of possible color superconducting phases that can arise in the cores of NSs, with the uncertainty arising from the unknown strong coupling at the densities within NSs. While the EoS used here are not constructed with the color superconducting gap parameter explicitly, the results obtained are still applicable to color superconducting stars in the limits of small pairing gaps, where the effects of color superconductivity at the EoS level may be minimal. The full results of exploring the effects of color superconductivity at the structural/EoS level will be reported elsewhere [7].

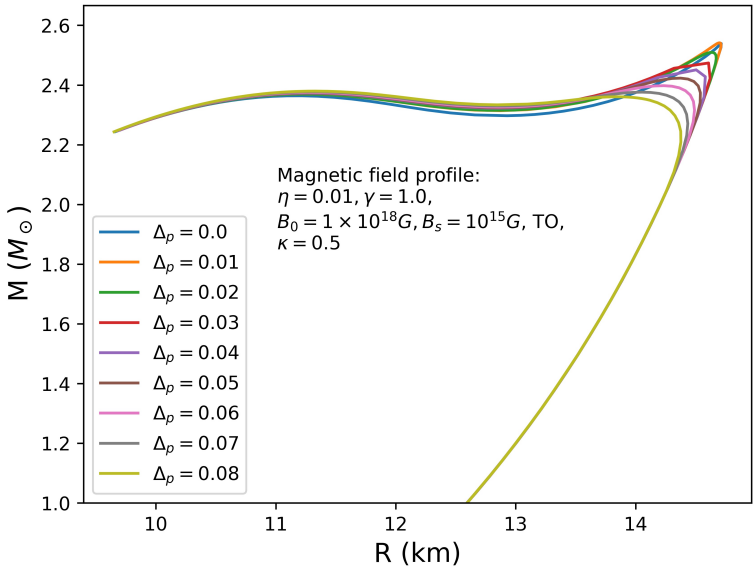


Figure 7. $M - R$ relation for ACB4 EoS with varying Δ_p and fixed magnetic field and anisotropy parameters.

2.4. Mass Gap Candidates

Although initially believed to be devoid of objects, in recent years, the "lower mass gap" between NSs and black holes is being filled by a number of GW and EM observations [35,36]. We examine the possibility that these mass gap objects, lying in the mass range ≈2–5 $M_\odot$, are in fact magnetized, anisotropic compact stars. In this work, we show that regardless of the constituent matter of the star—be it $npe\mu$ matter, $npe\mu - Y\Delta$ matter or even contain deconfined quarks—the combined effects of magnetic fields and anisotropy are able to enhance the star's mass and bring it to mass gap levels.

Some of the mass gap candidates identified from our selection of EoS ($npe\mu$, hybrid and $npe\mu - Y\Delta$ cases) have been listed in Table 1, with their relevant physical parameters. Thus, a mixture of magnetic field and anisotropy effects can enable NSs to attain mass gap range masses, even considering different matter constituents that make up the star.

Table 1. Possible mass gap candidates ($npe\mu$, $npe\mu - Y\Delta$ and hybrid EoS).

EoS	DDMEX ($npe\mu$)	DDMEX ($npe\mu - Y\Delta$)	ACB4 ($\Delta_p = 0.0$)	ACB4 ($\Delta_p = 0.0$)	DDMEX ($npe\mu - Y\Delta$)
$M_{\max}$ ($M_\odot$)	2.79	2.65	2.54	2.43	2.41
R (km)	12.91	13.24	14.71	14.5	12.84
ρ_c (MeV/fm^3)	837.06	762.61	572.15	572.15	882.03
B_c (10^{17} G)	7.69 (TO)	5.66 (TO)	2.24 (TO)	5.72 (TO)	7.85 (TO)
η, γ	0.01, 1	0.01, 1	0.01, 1	0.04, 0.9	0.05, 0.8
κ	0.3	0.5	0.5	0.3	0.15
$\frac{E_{\text{mag}}}{E_{\text{grav}}}$	0.03	0.018	0.006	0.053	0.055
$\Lambda_{1.4}$	510.61	422.04	333.82	453.05	614.03

3. Prospects for Detecting Neutron Stars Through Continuous Gravitational Waves

Continuous GWs (CGWs) provide a way to detect isolated NSs and to constrain their internal magnetic structure and dense matter EoS. Unlike transient signals from compact binary mergers, CGWs are long-duration quasi-monochromatic signals from rotating compact objects with a non-axisymmetric mass quadrupole [18]. As described in the previous section, in a magnetized anisotropic NS, magnetic stresses and anisotropic

pressures modify the hydrostatic balance. This can sustain a finite ellipticity that sources CGW emission.

In order to demonstrate the detectability of CGWs, in this section, the ellipticity ϵ is obtained from two-dimensional stationary axisymmetric equilibrium models computed with XNS. This is in contrast to the effective one-dimensional exploration in the previous section. While the structural analysis in Section 2 employs a one-dimensional modified TOV framework under approximate spherical symmetry, the ellipticity entering the CGW calculation is obtained from fully two-dimensional stationary axisymmetric equilibria. This ensures that magnetic-field-induced deformations are treated consistently when computing GW observables. We assume a mixed poloidal–toroidal magnetic configuration with toroidal dominance, consistent with arguments that stable large-scale stellar magnetic equilibria require a substantial toroidal component [26]. For the representative models used in Figure 8, we adopt a maximum internal toroidal field $B^{\rm tor}_{\rm max} = 5 \times 10^{15}$ G with the toroidal field near the surface approximately two orders of magnitude smaller, and a surface poloidal field at the pole $B_p = 10^{12}$ G.

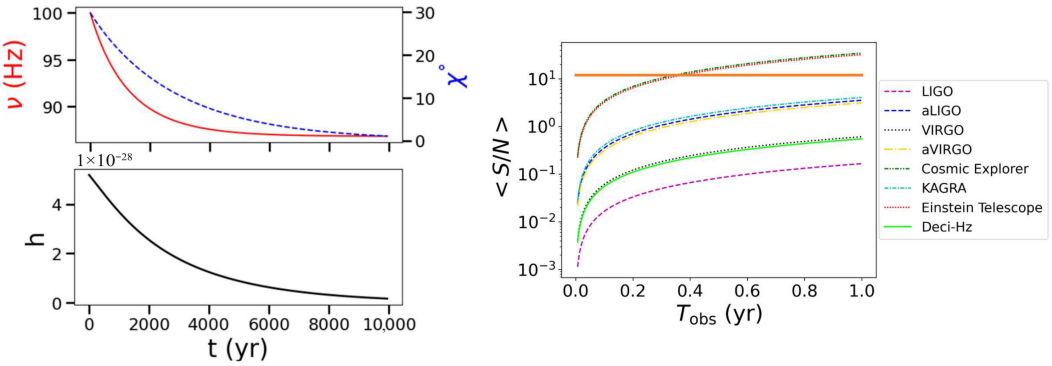


Figure 8. Evolution of CGW emission from a magnetically deformed rotating NS. (**Left panels**): temporal evolutions of spin frequency ν, obliquity angle χ, and resulting GW strain amplitude. (**Right panel**): cumulative SNR as a function of observation time for multiple detectors (aLIGO, aVirgo, KAGRA, Cosmic Explorer, Einstein Telescope, and Deci-Hz). The initial model uses $\nu_0 = 100$ Hz and $\chi_0 = 30^\circ$, and a toroidally dominated internal magnetic configuration with $B^{\rm tor}_{\rm max} = 5 \times 10^{15}$ G, surface toroidal field two orders of magnitude smaller, and polar surface poloidal field $B_p = 10^{12}$ G. The initial rise reflects coherent signal accumulation, while the later flattening indicates saturation caused by intrinsic strain decay during spin down. The orange horizontal line corresponds to SNR thresold = 12.

In this section, we illustrate detectability with representative instrument concepts spanning multiple frequency bands. For the example of signal-to-noise ratio (SNR) (Figure 8, right panel), we use the ground-based detectors aLIGO, aVirgo, and KAGRA; the third-generation detectors Cosmic Explorer and Einstein Telescope; and a representative space-based Deci-Hz design. Here, Deci-Hz is the proposed Indian Deci-Hz detector (Rajesh K. Nayak et al., private communication)[1]. For the characteristic strain sensitivity comparison (Figure 9), we use LISA, TianQin, ALIA, DECIGO, BBO, and Deci-Hz, which together cover roughly the 10^{-3}–10^{2} Hz range (with LISA and TianQin in the mHz band, DECIGO BBO and Deci-Hz in the decihertz band, and the transition toward ground based bands at higher frequencies).

A rotating NS emits CGWs when the symmetry axis of its mass distribution is misaligned with the rotation axis, characterized by the obliquity angle χ. In this case, the star possesses a time varying mass quadrupole moment that radiates GWs at harmonics of the spin frequency [18].

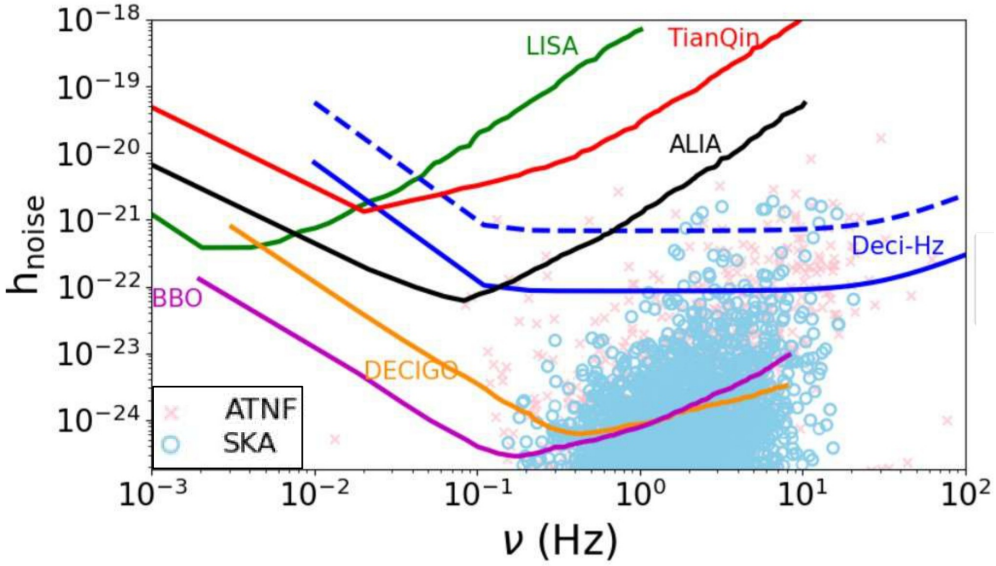


Figure 9. Characteristic strain h_c of ATNF pulsars and a projected SKA population along with sensitivity curves of some detectors (LISA, TianQin, ALIA, DECIGO, BBO, and Deci-Hz). The plot highlights that improved sensitivity in the decihertz band can enable detection of slowly rotating NSs via long-duration CGW searches.

The intrinsic GW amplitude h_0 denotes the characteristic strain produced by the source before the projection effects related to source orientation and detector response are included. For a rotating quadrupolar emitter, it is given by

$$h_0 = \frac{2G}{c^4}\frac{4\pi^2\nu^2\,\epsilon\,I_{xx}}{d}, \tag{5}$$

where ν is the spin frequency, I_{xx} is the principal moment of inertia, $\epsilon = |I_{zz} - I_{xx}|/I_{xx}$ is the ellipticity of the NS, and d is the source distance. The ellipticity depends on the stellar EoS and internal magnetic field configuration; toroidally dominated fields generally produce prolate distortions, whereas poloidal-dominated fields produce oblate configurations.

The observed GW strain h differs from h_0 because it depends on the source orientation relative to the observer. Specifically,

$$h = f(\chi, i)\,h_0, \tag{6}$$

where i is the inclination angle between the spin axis of the star and the line of sight, and $f(\chi, i)$ encodes the relative power distributed between emission at ν and 2ν. Following previous work [37], this geometric factor can be written as

$$f(\chi, i) = \frac{\sin\chi}{2\sqrt{2}}\left[(1+\cos^2 i)^2\sin^2\chi + 4\cos^2 i\cos^2\chi\right]^{1/2}(2\cos^2\chi - \sin^2\chi). \tag{7}$$

Since XNS computes stationary axisymmetric equilibria, the ellipticity ϵ is extracted directly from the equilibrium models, while the obliquity angle χ is introduced during post processing when computing the GW signal. When the orientation angles χ and i are unknown, we adopt the orientation averaged factor $\langle f\rangle_{i,\chi} \simeq 0.147$ following previous work [37].

For detection forecasts, the characteristic strain is the practical observable since it includes the effect of the integration time [38],

$$h_c = h_0\sqrt{\nu\,T_{\rm obs}}, \tag{8}$$

where $T_{\rm obs}$ denotes the observation time.

3.1. Evolutions of Spin and Obliquity

The CGW signal is intrinsically time-dependent because radiative torques extract angular momentum from the star, leading to the secular evolution of both the spin frequency and the obliquity angle. In addition to the GW torque (which depends on the deformation through $I_{zz} - I_{xx}$), EM dipole radiation from the extended poloidal field contributes to spin down through B_p. A convenient explicit form of the coupled evolution, showing where ϵ and B_p enter, is [37,39,40]

$$\left(\frac{\mathrm{d}\Omega}{\mathrm{d}t}\right)_{\rm rad} = -\frac{4B_p^2 R_p^6 \Omega^3}{c^3 I_{z'z'}}\left(1 + 1.1\sin^2\chi\right) - \frac{2G}{5c^5 I_{z'z'}}(I_{zz} - I_{xx})^2\Omega^5 \sin^2\chi\left(1 + 15\sin^2\chi\right), \tag{9}$$

$$I_{z'z'}\frac{\mathrm{d}\chi}{\mathrm{d}t} = -\frac{4B_p^2 R_p^6 \Omega^2}{c^3}\sin\chi\cos\chi - \frac{12G}{5c^5}(I_{zz} - I_{xx})^2\Omega^4 \sin^3\chi\cos\chi, \tag{10}$$

where R_p is the polar radius, $\Omega = 2\pi\nu$, I_{ij} are components of the moment of inertia tensor, and

$$I_{z'z'} = I_{zz}\cos^2\chi + I_{xx}\sin^2\chi. \tag{11}$$

Because $h_0 \propto \Omega^2$, spin down causes a progressive reduction in GW amplitude. Consequently, the detectability window is strongest at early times after formation. For the representative evolution shown in Figure 8, we adopt initial values $\nu_0 = 100$ Hz and $\chi_0 = 30^\circ$.

The coupled evolutions of spin frequency, obliquity angle, and GW strain are illustrated in Figure 8. The left panels show the evolutions of ν and χ together with the corresponding strain evolution, demonstrating how angular momentum loss drives a monotonic decay of the GW signal.

3.2. Signal to Noise Ratio

Detectability is quantified through SNR, which compares the accumulated GW signal power with the detector noise level [41,42]. For long-duration CGW searches, semi-coherent analyses divide the total observation time $T_{\rm obs}$ into $\mathcal{N}$ segments of duration $T_s = T_{\rm obs}/\mathcal{N}$. Accounting for emission at both the fundamental frequency ν and the harmonic 2ν, the cumulative SNR is

$$\langle \mathrm{SNR}\rangle = \sqrt{\langle \mathrm{SNR}_\nu^2\rangle + \langle \mathrm{SNR}_{2\nu}^2\rangle}, \tag{12}$$

where

$$\langle \mathrm{SNR}_\nu^2\rangle = \frac{\sin^2\zeta}{100}\sum_{s=1}^{\mathcal{N}}\frac{T_s h_0^2 \sin^2 2\chi}{S_n(\nu)}, \tag{13}$$

$$\langle \mathrm{SNR}_{2\nu}^2\rangle = \frac{4\sin^2\zeta}{25}\sum_{s=1}^{\mathcal{N}}\frac{T_s h_0^2 \sin^4\chi}{S_n(2\nu)}, \tag{14}$$

ζ is the interferometer arm opening angle and $S_n(\nu)$ is the power spectral density of detector noise. The angular dependence reflects how emissions at ν and 2ν project onto the detector response and determine the relative contribution of each harmonic to the accumulated signal. The resulting cumulative SNR evolution as a function of observation time for different detectors is shown in the right panel of Figure 8.

3.3. Detector Sensitivity and Pulsar Populations

Figure 9 compares characteristic strain sensitivity curves with the GW strain of known pulsars in the ATNF catalog [43] and projected SKA discoveries [44]. Sensitivity curves are

commonly compiled from publicly available detector design curves [38]. We include the ATNF pulsars to represent the currently known radio pulsar population, and we overlay the SKA population to illustrate the expected expansion of the observable pulsar sample from future surveys. This comparison provides an astrophysical context for where resent-day sources lie relative to detector sensitivity and how the enlarged SKA discovery space may populate regions that become accessible for CGW searches, especially in the decihertz band.

For pulsars in the ATNF catalog, we use the measured spin period P and period derivative $\dot{P}$ to estimate the surface dipolar field via the standard magnetic dipole spin-down relation

$$B_p \simeq 3.2 \times 10^{19} \sqrt{P\,\dot{P}}\,\mathrm{G}. \tag{15}$$

To relate observationally inferred dipolar fields to internal field strengths used to construct equilibrium models, we adopt the scaling $B_{\max} \approx 10^3\, B_p$ so that the internal maximum, possibly toroidal, field is taken to be three orders of magnitude larger than the estimated/inferred surface dipole field.

Within the anisotropic magnetized framework discussed in earlier sections, the key link to CGW detectability is the ellipticity ϵ, since it controls h_0 and therefore both h_c and the achievable SNR. A CGW detection would, therefore, provide an observational handle on internal magnetic structure and dense matter properties that is complementary to $M-R$ and tidal deformability constraints.

4. Influence of Magnetic Fields and Matter Anisotropy on White Dwarfs

WDs represent a lower compactness branch of relativistic stars where gravity is balanced by electron degeneracy pressure. In contrast to NSs, the spacetime curvature is weaker and, therefore, strong magnetic fields mainly alter the internal force balance through pressure splitting, rather than geometric deformation. For field strengths considered in this work, toroidal dominance preserves near-spherical equilibrium configuration, similar to as considered in Section 2. Hence the modified stellar structure equations already introduced through Equations (1) and (2) remain applicable and only the microscopic inputs differ.

4.1. Structure Equations with Magnetic Fields and Anisotropy

The interior of a carbon–oxygen WD is composed of a completely degenerate electron gas embedded in an ionic lattice. The matter pressure supporting the star arises from electron degeneracy and is described by the Chandrasekhar EoS expressed through the parameter $x = p_F/(m_e c)$, where p_F denotes the Fermi momentum, m_e the electron mass and c the speed of light. The radial matter pressure p_r and density ρ are given by

$$p_r = \frac{\pi m_e^4 c^5}{3h^3}\left[x(2x^2-3)\sqrt{x^2+1} + 3\sinh^{-1} x\right], \tag{16}$$

$$\rho = \frac{8\pi \mu_e m_H (m_e c)^3}{3h^3} x^3, \tag{17}$$

where h is the Planck constant, m_H is the hydrogen mass and $\mu_e = 2$ corresponds to the mean molecular weight. This EoS smoothly connects the non-relativistic and relativistic limits that occur across the WD interior. The effective density entering the equilibrium equations, defined earlier, is $\tilde{\rho} = \rho + B^2/8\pi$, where B represents the magnetic field strength. The pressure components appearing in Equation (2) follow the previously defined radial/parallel (RO) and transverse/perpendicular (TO) decompositions relative to the magnetic field direction. For the magnetic field range considered here, the magnetization energy density remains significantly smaller than the magnetic pressure contribution and is therefore neglected.

The anisotropic stress Δ in Equation (2) is the same as given by Equation (4) with the same interpretation and the range of κ. In magnetized WDs, this term represents the combined effect of magnetic tension and microscopic matter anisotropy. Inclusion of the matter-dependent contribution guarantees regular equilibrium at the stellar center where the total force must vanish.

Both the fossil magnetic field inherited from the progenitor star [45–47] and dynamo amplification during stellar evolution [48] lead to a strong central/internal magnetic field B_c, which gradually decreases towards a weaker surface value B_s. To mimic this spatial behavior, we adopt the same magnetic field distribution as given by Equation (3), except P replaced by ρ, as proposed originally [22,49]. However, for WDs we choose $\rho_0 = 10^9\,\mathrm{g\,cm^{-3}}$ and $\eta = 0.1$ and $\gamma = 1.8$. We take $B_s = 10^9$ G, consistent with observations of magnetic WDs [50].

For a chosen central density ρ_c, the integration begins with the boundary condition $m(0) = 0$ and proceeds outward until the radial pressure vanishes, which defines the stellar radius R. The interior solution is then matched to the Schwarzschild exterior metric, yielding the total mass $M = m(R)$. The resulting equilibrium configurations provide the mass radius ($M - R$) relation and the variation of anisotropy inside magnetized WD models.

4.2. Results and Physical Implications

We now examine how magnetic field strength, orientation, and matter anisotropy jointly determine the equilibrium configurations of magnetized WDs. Throughout the analysis, we fix the anisotropy parameter $\kappa = 0.45$, while the central field B_c is controlled through B_0. Different B_0 values are chosen for RO and TO because the Lorentz force contributes differently along and perpendicular to the field directions, producing asymmetric structural responses. For clarity, the principal structural quantities corresponding to the representative equilibrium configurations discussed in this section are summarized in Table 2. The table lists the maximum mass configuration for each magnetic geometry together with the corresponding radius, central density, central pressure, and compactness (Buchdahl value). These values are used below to quantitatively interpret the trends seen in the figures.

Table 2. Structural properties of magnetized white dwarfs for $\kappa = 0.45$, $\eta = 0.1$, $\gamma = 1.8$, and $B_s = 10^9$ G.

Orientation	B_0 (G)	$M_{\max}$ ($M_\odot$)	$R_{M_{\max}}$ (km)	B_c (G)	ρ_c (g cm^{-3})	P_c (Dyne cm^{-2})	Buchdahl
Transverse	1.955×10^{14}	2.10	1196.45	1.955×10^{14}	9.886×10^{9}	5.489×10^{28}	5.179×10^{-3}
	2.994×10^{14}	2.80	1200.80	2.994×10^{14}	9.206×10^{9}	2.479×10^{28}	6.880×10^{-3}
	0	1.65	927.90	0	2.569×10^{10}	9.865×10^{28}	5.252×10^{-3}
Radial	7.001×10^{12}	1.65	925.47	7.001×10^{12}	2.596×10^{10}	1.565×10^{30}	5.264×10^{-3}
	1.000×10^{13}	1.65	915.94	1.000×10^{13}	2.686×10^{10}	3.931×10^{30}	5.317×10^{-3}

Figure 10 shows the $M - R$ relations in the left panel together with the corresponding variation of M with ρ_c in the right panel. After the magnetic field is introduced, the stellar response separates according to field geometry, because the Lorentz force contributes differently in the parallel and perpendicular directions to the field. When the field is predominantly transverse (TO), the perpendicular magnetic pressure supplements the electron degeneracy pressure and counteracts gravity; therefore, the star expands, while its density decreases even though the mass increases. Quantitatively, the non-magnetized anisotropic configuration has $M_{\max} = 1.65\,M_\odot$, $R = 927.9$ km and $\rho_c = 2.569 \times 10^{10}\,\mathrm{g\,cm^{-3}}$ (see Table 2). This is purely the κ-effect increasing the mass above the $1.4\,M_\odot$ Chandrasekhar mass limit. For magnetized cases, we deliberately choose the values of $B_{0,TO}$

such that the models reproduce super-Chandrasekhar WDs (SCWDs) consistent with overluminous SNe Ia such as SN 2003fg (corresponds to $\sim$2.1 $M_\odot$) and SN 2009dc (corresponds to $\sim$2.8 $M_\odot$). For $B_{0,TO} = 1.959 \times 10^{14}$ G the maximum mass rises to 2.1 $M_\odot$ with $R = 1196.5$ km and $\rho_c = 9.886 \times 10^9$ g cm^{-3} (see Table 2). Increasing the field further so that $B_{0,TO} = 3.007 \times 10^{14}$ G produces $M_{\max} = 2.8\, M_\odot$ and $R = 1200.8$ km with $\rho_c = 9.206 \times 10^9$ g cm^{-3} and the corresponding pressure $P_c = 2.483 \times 10^{28}$ dyne cm^{-2}. The compactness remains small, which is 6.88×10^{-3} for the latter. This demonstrates that the additional support arises from magnetic pressure rather than relativistic gravitational compression, so the configuration becomes super-Chandrasekhar yet remains weakly relativistic compared to NSs and even WDs closer to the Chandrasekhar mass limit in the absence of magnetic fields and anisotropies. In contrast, RO aligns the magnetic tension with gravity and, therefore, enhances the inward force. The degeneracy pressure must then grow to balance gravity, which leads to strong compression with only a minor change in total mass when there appears to be an upper limit of ρ_c in order to avoid gravitational instability. For $B_{0,RO} = 0.07 \times 10^{14}$ G the mass is 1.65 $M_\odot$ but the radius contracts to 925.47 km (see Table 2). For $B_{0,RO} = 0.1 \times 10^{14}$ G the radius further decreases to 915.94 km, while the mass remains the same as 1.65 $M_\odot$. Hence, it is clear that such low fields do not affect the mass, but only the radius.

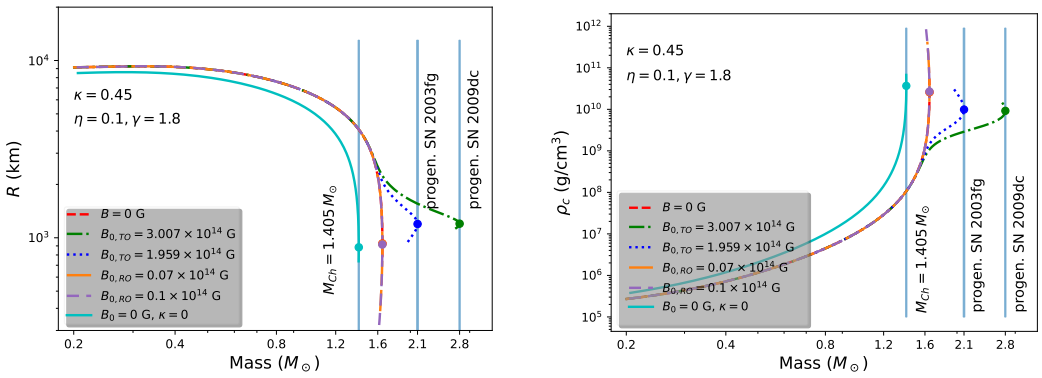


Figure 10. (**Left panel**): the mass–radius relation for different magnetic strengths and orientations. (**Right panel**): the corresponding dependence on central density.

The present models are constructed using the Chandrasekhar EoS for carbon–oxygen (CO) WDs and are intended to isolate the structural impact of magnetic geometry and anisotropic stresses. At central densities above 10^{10} g cm^{-3}, additional microphysical processes such as electron captures, neutronization, and eventual neutron drip become increasingly important and would modify EoS. The RO configurations are, therefore, restricted to this density regime, which effectively places an upper bound on the admissible central magnetic field in such models. Within this framework, the solutions represent controlled magneto–hydrostatic equilibria that illustrate the compressive effect of magnetic tension while remaining broadly consistent with the density range expected for WD interiors. The monotonic increase in M with ρ_c up to the turning point in the right panel of Figure 10 indicates that the configurations lie on a stable equilibrium branch, consistent with the standard stability criterion $dM/d\rho_c > 0$. The contrasting behavior between the two field geometries follows directly from the direction of the Lorentz force. TO fields provide an additional pressure component perpendicular to gravity, allowing the star to support larger masses at comparatively lower central densities. In contrast, RO fields align magnetic tension with gravity, leading to enhanced inward compression and significantly higher central densities with only modest changes in total mass, particularly if we restrict strictly ρ_c by an upper limit. Thus, TO configurations naturally produce massive, low-density WDs, whereas RO configurations yield compression-dominated equilibria that are more compact

and closer to the Chandrasekhar mass limit, with any deviation arising from anisotropic effects other than magnetic fields.

Figure 11 simultaneously demonstrates how the maximum mass of a $M - R$ relation $M_{\rm max}$ and the magnetic to gravitational energy ratio $E_{\rm mag}/E_{\rm grav}$ evolve with the central magnetic field strength (B_c) and, therefore, directly reveals the mechanism by which field geometry controls stellar support. The left panel of Figure 11 presents the variation of $M_{\rm max}$ with B_c while the right panel shows the corresponding behavior of the energy ratio $E_{\rm mag}/E_{\rm grav}$. At weak fields, both orientations behave almost identically because magnetic stresses are weak compared to electron degeneracy pressure and gravity, so the models converge to $M_{\rm max} \approx 1.65\,M_\odot$. The deviation from the Chandrasekhar mass limit is due to anisotropic effects. This is verified numerically since for B_c up to a few factors times $\sim 10^{11}$ G, both the TO and RO cases give a similar mass, close to $1.65\,M_\odot$, and the right panel shows that the energy ratio remains extremely small with $E_{\rm mag}/E_{\rm grav} \approx 10^{-7}$. In the present analysis, we restrict the choice of $B_{0,TO}$ and $B_{0,RO}$ such that the resulting equilibrium configurations remain within the physically relevant WD density regime, specifically $\rho_c \sim 10^{10}\,{\rm g\,cm^{-3}}$. As the field increases, the behavior between TO and RO cases separates. As discussed above, for TO, the star can support more mass without requiring higher density. The left panel of Figure 11, therefore, shows a monotonic rise in mass with B_c, while the density decreases, as already shown in Figure 10. Quantitatively $M_{\rm max}$ remains almost unchanged up to $B_c \sim 10^{13}$ G with $M_{\rm max} \approx 1.65\,M_\odot$, but beyond this threshold, magnetic pressure becomes dynamically relevant and the mass rises rapidly, reaching $1.94\,M_\odot$ at 1.59×10^{14} G, then $2.12\,M_\odot$ at 1.99×10^{14} G, and finally $2.88\,M_\odot$ at 3.09×10^{14} G. The right panel shows that the accompanying energy ratio grows from $\sim 10^{-7}$ at low fields to $\sim 10^{-1}$ at the highest fields considered, which remains below unity but can reach $\mathcal{O}(10^{-1})$ in the strongest field configurations, showing that gravity still dominates global binding, and, therefore, the configurations remain stable while allowing SCWD masses. This behavior is consistent with the classical stability argument of Chandrasekhar and Fermi [51], who demonstrated that for magnetized compact stars the usual relativistic stability condition $\Gamma > 4/3$ is not sufficient and that dynamical stability additionally requires $E_{\rm mag}/|E_{\rm grav}| \ll 1$. In contrast, for RO, the star must increase the degeneracy pressure to overcome the combined effects of the magnetic field and gravity, so the density rises while the mass changes little. The left panel of Figure 11, therefore, shows a gradual decrease of mass from $\sim 1.65\,M_\odot$ at 2×10^{13} G to $\sim 1.61\,M_\odot$ at 1.33×10^{14} G, even though ρ_c grows by more than an order of magnitude. The right panel shows that the corresponding energy ratio also increases but much more slowly, remaining near $\sim \times 10^{-3}$ at the largest field, which confirms that magnetic energy mainly reshapes the internal structure rather than providing global support. The combined interpretation of the two panels is, therefore, clear. TO fields increase stellar mass by providing an additional pressure component, whereas RO fields primarily compress the star. The smooth monotonic trends and the fact that $E_{\rm mag}/E_{\rm grav}$ remains below unity throughout both sequences demonstrate that all equilibrium solutions remain gravitationally bound and physically stable, while only the TO configuration can naturally produce SCWDs (any SCWDs in RO is due to matter anisotropy).

The left panel of Figure 12 shows the dependence of the maximum gravitational mass on the magnetic profile index γ, with the color scale representing the volume-averaged magnetic pressure fraction $\langle P_B\rangle/\langle P_{\rm tot}\rangle$. In this calculation, $\eta = 0.1$ and $B_{0,TO} = 3.007 \times 10^{14}$ G, are fixed, while γ is varied. A clear monotonic trend emerges: for $\gamma \approx 0.9$, the sequence begins at $M_{\rm max} \approx 1.9\,M_\odot$ with a modest magnetic contribution $\langle P_B\rangle/\langle P_{\rm tot}\rangle \approx 0.1$. As γ increases, the field becomes more concentrated toward higher-density regions, and $M_{\rm max}$ rises smoothly beyond $2\,M_\odot$, reaching nearly $3\,M_\odot$ for $\gamma \gtrsim 1.9$, while $\langle P_B\rangle/\langle P_{\rm tot}\rangle$ increases to $\gtrsim 0.3$.

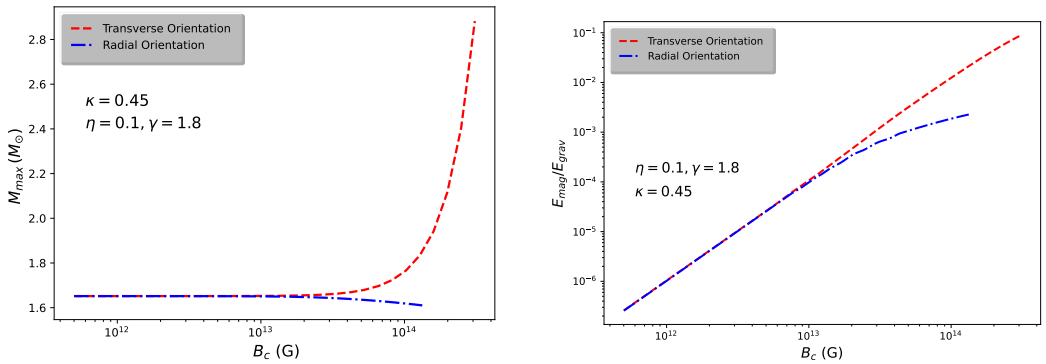


Figure 11. (**Left panel**): the variation of maximum mass with central magnetic field. (**Right panel**): the magnetic to gravitational energy ratio demonstrating stability of the configurations.

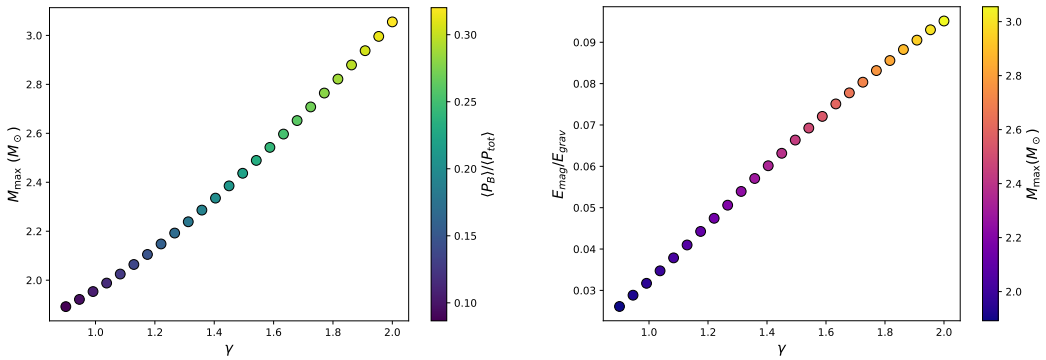


Figure 12. (**Left panel**): The variation of the maximum mass $M_{\max}$ with magnetic profile index γ for fixed $\eta = 0.1$ and $B_{0,TO} = 3.007 \times 10^{14}$ G, where color shows the volume-averaged magnetic pressure fraction $\langle P_B \rangle / \langle P_{\rm tot} \rangle$, indicating increasing magnetic pressure support and emergence of SCWD configurations. (**Right panel**): The variation of the magnetic to gravitational energy ratio $E_{\rm mag}/E_{\rm grav}$ with γ, where color showing $M_{\max}$.

Since γ controls the density dependence of the magnetic field, larger values enhance magnetic stresses where gravity is strongest. The resulting mass increase, therefore, reflects a redistribution of the internal force balance, rather than a transition to magnetic domination. The smooth behavior without turning points indicates a continuous modification of the hydrostatic equilibrium, leading naturally to super-Chandrasekhar configurations that remain gravitationally bound.

The right panel of Figure 12 displays the variation in $E_{\rm mag}/E_{\rm grav}$ as the magnetic profile index γ changes, while the color scale indicates the corresponding maximum mass configuration. Note that for this entire analysis, $\eta = 0.1$ and $B_{0,TO} = 3.007 \times 10^{14}$ G are maintained. Interestingly, a notable feature is that the energy ratio increases from $\sim 2.6 \times 10^{-2}$ to nearly $\sim 10^{-1}$ across the range $0.9 \leq \gamma \leq 2.0$. At lower γ, the configurations that produce $M_{\max} \approx 1.9\, M_\odot$ already possess a small but nonzero magnetic contribution to the global energy budget. As γ increases, $M_{\max}$ grows continuously and exceeds $3\, M_\odot$, yet the energy ratio increases more gradually and remains within the same order of magnitude. The plot, therefore, shows that even when the supported mass increases substantially, the total magnetic energy remains well below the gravitational binding energy. This behavior indicates that the role of the magnetic field is not to dominate the global energetics but rather to redistribute forces within the star. Since γ controls how strongly the magnetic field is concentrated toward the higher density regions, increasing γ enhances the effectiveness of magnetic stresses in the interior while requiring only a moderate increase in total magnetic energy. Consequently, configurations with larger masses correspond to the values of $E_{\rm mag}/E_{\rm grav}$ comparable to those of smaller masses, because the magnetic

field acts locally where gravity is strongest rather than uniformly throughout the volume. The absence of any sharp growth or divergence in the ratio across the sequence further suggests that the solutions remain gravitationally bound over the explored parameter space. Thus, the right panel of Figure 12 implies that SCWDs arise from the spatial distribution of magnetic support rather than from a globally dominant magnetic energy reservoir.

Overall, the combined action of magnetic geometry, matter anisotropy, and magnetic profile determines the structural behavior of magnetized WDs. The TO fields allow the star to support increasingly larger masses, including SCWD configurations, while the RO fields mainly modify the compactness by enhancing compression with a comparatively small change in mass. The γ-dependent analysis further shows that the growth of the supported mass does not require a comparable growth of the global magnetic energy; instead, the ratio $E_{\rm mag}/E_{\rm grav}$ increases gradually while remaining well below unity. This indicates that magnetic fields primarily alter the internal force distribution rather than the overall binding energetics. Consequently, the configurations remain gravitationally bound and stable, and SCWD masses arise from the spatial organization of magnetic stresses rather than from a magnetically dominated star.

For large poloidal magnetic field strengths, the associated dipole luminosity can be very high. This leads to a rapid decrease in the pulsar inclination angle, which in turn reduces the GW amplitude. In such a case, a fully coherent integration over long durations is no longer appropriate. Instead, the data needs to be segmented into shorter intervals of duration $T_{\rm stack}$ within which Ω can be considered approximately constant. The total observation time $T_{\rm obs}$ can thus be written as $T_{\rm obs} = \mathcal{N} T_{\rm stack}$, where $\mathcal{N}$ is the number of stacks. Assuming ν, χ and h_0 remain approximately constant in each time stack $T_{\rm stack}$, adding $\mathcal{N}$ such stacks, the new cumulative SNRs for this incoherent search are given by

$$\langle {\rm SNR}^2_{\nu} \rangle = \frac{\sin^2\zeta}{100} \frac{h_0^2 \sqrt{\mathcal{N}} T_{\rm stack} \sin^2 2\chi}{S_{\rm n}(\nu)} = \frac{\sin^2\zeta}{100} \frac{h_0^2 T_{\rm obs} \sin^2 2\chi}{\sqrt{\mathcal{N}} S_{\rm n}(\nu)} \tag{18}$$

$$\langle {\rm SNR}^2_{2\nu} \rangle = \frac{4\sin^2\zeta}{25} \frac{h_0^2 \sqrt{\mathcal{N}} T_{\rm stack} \sin^4 \chi}{S_{\rm n}(2\nu)} = \frac{4\sin^2\zeta}{25} \frac{h_0^2 T_{\rm obs} \sin^4 \chi}{\sqrt{\mathcal{N}} S_{\rm n}(2\nu)}. \tag{19}$$

This is particularly useful for arbitrary WD search, unlike the targeted search proposed for NSs. We consider stacking duration $T_{\rm stack} = 1\,$h. Additionally, a detection criterion of $\langle {\rm S/N} \rangle \gtrsim 5$ is adopted, corresponding to a detection efficiency exceeding 95% [52].

We consider a typical WD with a maximum internal toroidal magnetic field strength of approximately $B_{\rm max} = 2.6 \times 10^{14}\,$G. With the XNS code, it is not possible to construct a WD with a suitably chosen mixed-field configuration. Therefore, we assume that such a configuration is accompanied by a surface poloidal field approximately four orders of magnitude weaker than $B_{\rm max}$ following [53]. This weaker poloidal component has a negligible effect on the stellar structure compared to the dominant toroidal field. Figure 13 presents the cumulative SNR for a WD with $B_{\rm max} = 2.6 \times 10^{14}\,$G with a mass of $1.7\,M_\odot$. Under these conditions, all considered GW detectors, except LISA, are capable of detecting the source almost instantaneously, while LISA achieves detection within approximately five months of integration time.

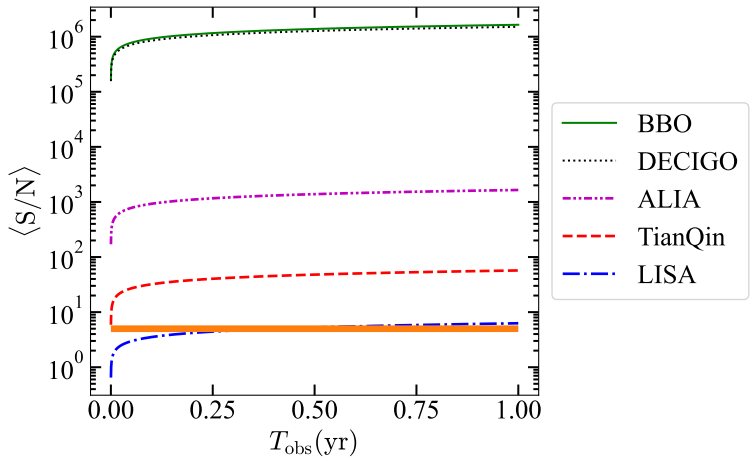


Figure 13. Cumulative SNR as a function of observed period for a typical toroidally dominated super-Chandrasekhar WD, characterized by a maximum internal magnetic field strength of approximately 2.6×10^{14} G, with the surface magnetic field assumed to be nearly four orders of magnitude lower. The bold orange line corresponds to the detection threshold SNR = 5.

5. Conclusions

In this invited review, we have presented a unified treatment of magnetically induced anisotropy in compact stars, connecting microphysical modeling of dense matter to macroscopic structure and multimessenger observables. By incorporating anisotropic stresses arising from strong magnetic fields and matter effects into modified stellar structure equations, we have explored NSs, hybrid stars, and WDs within a common framework.

For NSs, we have demonstrated that magnetic-field geometry plays a decisive role in determining global properties. Toroidally oriented (transverse) fields enhance the maximum mass by providing additional perpendicular pressure support, whereas radially oriented fields primarily increase central compression with comparatively smaller mass gain. In hybrid configurations, anisotropy shifts the mass at which the hadron–quark phase transition occurs, raising the hadronic branch to larger masses before the quark core becomes energetically favorable. These effects allow magnetized, anisotropic NSs to reach masses within the lower mass gap without requiring magnetic energy to dominate gravitational binding.

We have further shown that CGW emission from magnetically deformed NSs offers a complementary probe of internal magnetic structure. The ellipticity derived from two-dimensional axisymmetric equilibrium configurations connects internal field geometry directly to observable strain amplitudes, providing an independent constraint on dense-matter properties beyond mass–radius and tidal-deformability measurements.

In magnetized WDs, the interplay between magnetic geometry and anisotropic stresses determines whether magnetic fields primarily increase mass (for transverse configurations) or enhance compression (for radial configurations). Super-Chandrasekhar configurations arise from the redistribution of magnetic stresses within the star rather than from magnetic domination of the global energy budget, as $E_{\rm mag}/|E_{\rm grav}|$ remains well below unity in all stable solutions.

Across all classes of compact stars considered here, a central result emerges: magnetic-field geometry, through its control of anisotropic stresses, is as important as field strength in shaping observable properties. The combined influence of magnetic stresses and matter anisotropy modifies $M - R$ relations, tidal deformability, phase-transition thresholds, and GW emission in a coherent and physically transparent manner. Future work incorporating detailed microphysics and fully dynamical magnetohydrodynamic stability analyses

will be essential to determine the extent to which these anisotropic configurations can be realized in astrophysical environments.

Author Contributions: Z.Z. performed the calculations and wrote the section of the draft on anisotropic neutron stars and hybrid stars. M.D. performed the calculations and wrote the section concerning continuous gravitational waves from neutron stars. D.D. performed the calculations, developed the analysis, and wrote the section on magnetized anisotropic white dwarfs. S.K. performed the signal-to-noise ratio modeling for the super-Chandrasekhar white dwarfs. F.W. contributed to the methodology, original plan and editing the draft. B.M. defined the problem and methodology, wrote the Introduction and Conclusions, checked and refined all the results reported in the sections by the coauthors, tied them up coherently, and overall supervised the project. All authors have read and agreed to the published version of the manuscript.

Funding: Z.Z. is supported by the Prime Minister's Research Fellows (PMRF) scheme, Ref. No. TF/PMRF-22-7307. M.D. acknowledges PMRF scheme, Ref. No. TF/PMRF-22-5442.03 for support. S.K. acknowledges funding from the National Science Centre (NCN), Poland with grant no. 2023/49/B/ST9/02777.

Data Availability Statement: The data used in this study will be made available on reasonable request.

Acknowledgments: B.M. and M.D. thank Manjari Bagchi and Arunava Mukherjee for fruitful discussion about CGW population.

Conflicts of Interest: The authors declare no conflicts of interest.

Note

[1] Based on representative noise power spectral density (PSD) of a possible Indian deciHz mission, tentatively referred to as IndIGO-D.

References

1. Kaspi, V.; Beloborodov, A. Magnetars. *Ann. Rev. Astron. Astrophys.* **2017**, *55*, 261–301. [CrossRef]
2. Ferrario, L.; Wickramasinghe, D.; Kawka, A. Magnetic fields in isolated and interacting white dwarfs. *Adv. Space Res.* **2020**, *66*, 1025–1056. [CrossRef]
3. Das, U.; Mukhopadhyay, B. Revisiting some physics issues related to the new mass limit for magnetized white dwarfs. *Mod. Phys. Lett. A* **2014**, *29*, 1450035. [CrossRef]
4. Deb, D.; Mukhopadhyay, B.; Weber, F. Effects of Anisotropy on Strongly Magnetized Neutron and Strange Quark Stars in General Relativity. *Astrophys. J.* **2021**, *922*, 149. [CrossRef]
5. Das, M.; Sedrakian, A.; Mukhopadhyay, B. Superconductivity in magnetars: Exploring type-I and type-II states in toroidal magnetic fields. *Phys. Rev. D* **2025**, *111*, L081307.
6. Das, M.; Sedrakian, A.; Mukhopadhyay, B. Topology of the superconducting heart of neutron stars: Effects of microphysics and gravitational-wave signatures. *Phys. Rev. D* **2026**, *113*, 043004.
7. Zuraiq, Z.; Mukhopadhyay, B. Anisotropic hybrid stars: Interplay of superconductivity and magnetic field leading to gravitational waves. *arXiv* **2026**, arXiv:2604.06308. [CrossRef]
8. Herrera, L.; Santos, N. Local anisotropy in self-gravitating systems. *Phys. Rep.* **1997**, *286*, 53–130. [CrossRef]
9. Herrera, L. Stability of the isotropic pressure condition. *Phys. Rev. D* **2020**, *101*, 104024.
10. Taubenberger, S.; Benetti, S.; Childress, M.; Pakmor, R.; Hachinger, S.; Mazzali, P.; Stanishev, V.; Elias-Rosa, N.; Agnoletto, I.; Bufano, F.; et al. High luminosity, slow ejecta and persistent carbon lines: SN 2009dc challenges thermonuclear explosion scenarios. *Mon. Not. R. Astron. Soc.* **2011**, *412*, 2735–2762. [CrossRef]
11. Andrew Howell, D.; Sullivan, M.; Nugent, P.E.; Ellis, R.S.; Conley, A.J.; Le Borgne, D.; Carlberg, R.G.; Guy, J.; Balam, D.; Basa, S.; et al. The type Ia supernova SNLS-03D3bb from a super-Chandrasekhar-mass white dwarf star. *Nature* **2006**, *443*, 308–311. [CrossRef]
12. Das, U.; Mukhopadhyay, B. Modified Einstein's gravity as a possible missing link between sub- and super-Chandrasekhar type Ia supernovae. *J. Cosmol. Astropart. Phys.* **2015**, *2015*, 045. [CrossRef]
13. Belyaev, V.B.; Ricci, P.; Šimkovic, F.; Adam, J.; Tater, M.; Truhlík, E. Consequence of total lepton number violation in strongly magnetized iron white dwarfs. *Nuc. Phys. A* **2015**, *937*, 17–43. [CrossRef]

14. Lai, D.; Shapiro, S.L. Cold Equation of State in a Strong Magnetic Field: Effects of Inverse beta-Decay. *Astrophys. J.* **1991**, *383*, 745–751. [CrossRef] [PubMed]
15. Vishal, M.V.; Mukhopadhyay, B. Revised density of magnetized nuclear matter at the neutron drip line. *Phys. Rev. C* **2014**, *89*, 065804. [CrossRef]
16. Das, U.; Mukhopadhyay, B. New Mass Limit for White Dwarfs: Super-Chandrasekhar Type Ia Supernova as a New Standard Candle. *Phys. Rev. Lett.* **2013**, *110*, 071102. [CrossRef]
17. Kalita, S.; Mukhopadhyay, B. Modified Einstein's gravity to probe the sub- and super-Chandrasekhar limiting mass white dwarfs: A new perspective to unify under- and over-luminous type Ia supernovae. *J. Cosmol. Astropart. Phys.* **2018**, *2018*, 007. [CrossRef]
18. Bonazzola, S.; Gourgoulhon, E. Gravitational waves from pulsars: Emission by the magnetic field induced distortion. *Astron. Astrophys.* **1996**, *312*, 675.
19. Kalita, S.; Mukhopadhyay, B. Continuous gravitational wave from magnetized white dwarfs and neutron stars: Possible missions for LISA, DECIGO, BBO, ET detectors. *Mon. Not. R. Astron. Soc.* **2019**, *490*, 2692–2705. [CrossRef]
20. Zuraiq, Z.; Mukhopadhyay, B.; Weber, F. Massive neutron stars as mass gap candidates: Exploring equation of state and magnetic field. *Phys. Rev. D* **2024**, *109*, 023027. [CrossRef]
21. Deb, D.; Mukhopadhyay, B.; Weber, F. Anisotropic Magnetized White Dwarfs: Unifying Under- and Overluminous Peculiar and Standard Type Ia Supernovae. *Astrophys. J.* **2022**, *926*, 66. [CrossRef]
22. Bandyopadhyay, D.; Chakrabarty, S.; Pal, S. Quantizing magnetic field and quark-hadron phase transition in a neutron star. *Phys. Rev. Lett.* **1997**, *79*, 2176–2179. [CrossRef]
23. Bowers, R.; Liang, E. Anisotropic Spheres in General Relativity. *Astrophys. J.* **1974**, *188*, 657–665. [CrossRef]
24. Silva, H.; Macedo, C.; Berti, E.; Crispino, L. Slowly rotating anisotropic neutron stars in general relativity and scalar–tensor theory. *Class. Quant. Grav.* **2015**, *32*, 145008. [CrossRef]
25. Pili, A.; Bucciantini, N.; Del Zanna, L. Axisymmetric equilibrium models for magnetized neutron stars in General Relativity under the Conformally Flat Condition. *Mon. Not. R. Astron. Soc.* **2014**, *439*, 3541–3563. [CrossRef]
26. Braithwaite, J. Axisymmetric magnetic fields in stars: Relative strengths of poloidal and toroidal components. *Mon. Not. R. Astron. Soc.* **2009**, *397*, 763–774. [CrossRef]
27. Abbott, B.P.; Abbott, R.; Abbott, T.D.; Acernese, F.; Ackley, K.; Adams, C.; Adams, T.; Addesso, P.; Adhikari, R.X.; Adya, V.B.; et al. GW170817: Measurements of Neutron Star Radii and Equation of State. *Phys. Rev. Lett.* **2018**, *121*, 161101. [CrossRef]
28. Abbott, B.P.; Abbott, R.; Abbott, T.D.; Acernese, F.; Ackley, K.; Adams, C.; Adams, T.; Addesso, P.; Adhikari, R.X.; Adya, V.B.; et al. GW170817: Observation of Gravitational Waves from a Binary Neutron Star Inspiral. *Phys. Rev. Lett.* **2017**, *119*, 161101. [CrossRef]
29. Taninah, A.; Agbemava, S.; Afanasjev, A.; Ring, P. Parametric correlations in energy density functionals. *Phys. Lett. B* **2020**, *800*, 135065. [CrossRef]
30. Typel, S.; Röpke, G.; Klähn, T.; Blaschke, D.; Wolter, H. Composition and thermodynamics of nuclear matter with light clusters. *Phys. Rev. C.* **2010**, *81*, 015803. [CrossRef]
31. Lalazissis, G.A.; Nikšić, T.; Vretenar, D.; Ring, P. New relativistic mean-field interaction with density-dependent meson-nucleon couplings. *Phys. Rev. C* **2005**, *71*, 024312. [CrossRef]
32. Weber, F. Strange quark matter and compact stars. *Prog. Part. Nucl. Phys.* **2005**, *54*, 193–288. [CrossRef]
33. Blaschke, D.; Alvarez-Castillo, D.; Ayriyan, A.; Grigorian, H.; Largani, N.; Weber, F. Astrophysical aspects of general relativistic mass twin stars. In *Topics on Strong Gravity: A Modern View on Theories and Experiments*; World Scientific: Singapore, 2020; pp. 207–256.
34. Alford, M.; Rajagopal, K.; Reddy, S.; Wilczek, F. Minimal color-flavor-locked-nuclear interface. *Phys. Rev. D.* **2001**, *64*, 074017. [CrossRef]
35. Abbott, R.; Abbott, T.D.; Abraham, S.; Acernese, F.; Ackley, K.; Adams, C.; Adhikari, R.X.; Adya, V.B.; Affeldt, C.; Agathos, M.; et al. GW190814: Gravitational Waves from the Coalescence of a 23 Solar Mass Black Hole with a 2.6 Solar Mass Compact Object. *Astrophys. J. Lett.* **2020**, *896*, L44. [CrossRef]
36. Barr, E.D.; Dutta, A.; Freire, P.C.; Cadelano, M.; Gautam, T.; Kramer, M.; Pallanca, C.; Ransom, S.M.; Ridolfi, A.; Stappers, B.W.; et al. A pulsar in a binary with a compact object in the mass gap between neutron stars and black holes. *Science* **2024**, *383*, 275–279. [CrossRef]
37. Das, M.; Mukhopadhyay, B.; Bulik, T. Continuous gravitational waves from magnetized white dwarfs: Quantifying the detection plausibility by LISA. *Astrophys. J.* **2025**, *995*, 107. [CrossRef]
38. Moore, C.J.; Cole, R.H.; Berry, C.P.L. Gravitational wave sensitivity curves. *Class. Quantum Grav.* **2015**, *32*, 015014. [CrossRef]
39. Chau, W.Y.; Henriksen, R.N. Alignment of an oblique spheroidal rotator through electromagnetic and gravitational radiation. *Astrophys. J.* **1970**, *161*, L137. [CrossRef]
40. Das, M.; Mukhopadhyay, B. Detection Possibility of Continuous Gravitational Waves from Rotating Magnetized Neutron Stars. *Astrophys. J.* **2023**, *955*, 19. [CrossRef]

41. Jaranowski, P.; Królak, A.; Schutz, B.F. Data analysis of gravitational wave signals from spinning neutron stars. *Phys. Rev. D* **1998**, *58*, 063001. [CrossRef]
42. Bennett, M.F.; van Eysden, C.A.; Melatos, A. Continuous-wave gravitational radiation from pulsar glitch recovery. *Mon. Not. R. Astron. Soc.* **2010**, *409*, 1705–1718. [CrossRef]
43. Manchester, R.N.; Hobbs, G.B.; Teoh, A.; Hobbs, M. The Australia Telescope National Facility Pulsar Catalogue. *Astron. J.* **2005**, *129*, 1993–2006. [CrossRef]
44. Levin, L.; Bagchi, M.; Burgay, M.; Deller, A.T.; Graber, V.; Igoshev, A.; Kramer, M.; Lorimer, D.; Posselt, B.; Prabu, T.; et al. Understanding the neutron star population with the SKAO telescopes. *Open J. Astrophys.* **2025**, *8*, 54653. [CrossRef]
45. Fujisawa, K.; Yoshida, S.; Eriguchi, Y. Axisymmetric and stationary structures of magnetized barotropic stars with extremely strong magnetic fields deep inside. *Mon. Not. R. Astron. Soc.* **2012**, *422*, 434–448. [CrossRef]
46. Das, U.; Mukhopadhyay, B. Maximum mass of stable magnetized highly super-Chandrasekhar white dwarfs: Stable solutions with varying magnetic fields. *J. Cosmol. Astropart. Phys.* **2014**, *2014*, 050. [CrossRef]
47. Subramanian, S.; Mukhopadhyay, B. GRMHD formulation of highly super-Chandrasekhar rotating magnetized white dwarfs: Stable configurations of non-spherical white dwarfs. *Mon. Not. R. Astron. Soc.* **2015**, *454*, 752–765. [CrossRef]
48. Potter, A.T.; Tout, C.A. Magnetic field evolution of white dwarfs in strongly interacting binary star systems. *Mon. Not. R. Astron. Soc.* **2010**, *402*, 1072–1080. [CrossRef]
49. Bandyopadhyay, D.; Pal, S.; Chakrabarty, S. Protoneutron star in a strongly quantizing magnetic field. *J. Phys. G* **1998**, *24*, 1647–1649. [CrossRef]
50. Schmidt, G.D.; Harris, H.C.; Liebert, J.; Eisenstein, D.J.; Anderson, S.F.; Brinkmann, J.; Hall, P.B.; Harvanek, M.; Hawley, S.; Kleinman, S.J.; et al. Magnetic white dwarfs from the Sloan Digital Sky Survey: The first data release. *Astrophys. J.* **2003**, *595*, 1101–1113. [CrossRef]
51. Chandrasekhar, S.; Fermi, E. Problems of gravitational stability in the presence of a magnetic field. *Astrophys. J.* **1953**, *118*, 116–141. [CrossRef]
52. Pitkin, M. Prospects of observing continuous gravitational waves from known pulsars. *Mon. Not. R. Astron. Soc.* **2011**, *415*, 1849–1863. [CrossRef]
53. Kalita, S.; Mondal, T.; Tout, C.A.; Bulik, T.; Mukhopadhyay, B. Resolving dichotomy in compact objects through continuous gravitational waves observation. *Mon. Not. R. Astron. Soc.* **2011**, *508*, 842–851. [CrossRef]

Disclaimer/Publisher's Note: The statements, opinions and data contained in all publications are solely those of the individual author(s) and contributor(s) and not of MDPI and/or the editor(s). MDPI and/or the editor(s) disclaim responsibility for any injury to people or property resulting from any ideas, methods, instructions or products referred to in the content.